

GENERAL DESIGN CONSIDERATIONS FOR SOLAR-ELECTRIC HIGH-ALTITUDE LONG-ENDURANCE AIRCRAFT

Andreas Bierig¹, Florian Nikodem¹, Daniel Rothe¹

¹German Aerospace Center (DLR), Lilienthalplatz 7, 38108 Braunschweig

Abstract

Solar-electric stratospheric aircraft represent an interesting alternative to low Earth orbit satellites. They can be easily launched and landed, causing no pollution to the atmosphere and leaving no space debris. The design of such aircraft remains a significant challenge even today. Due to advancements in solar cell technology, lithium-ion batteries, and lightweight materials for aircraft structures, it is now possible to deploy such aircraft, which could cover a wide operational range in the future. Fundamentally, the design of such aircraft requires consideration of various physical relationships that indicate operational limits and technological development needs. This publication, based on a model of environmental conditions and fundamental flight performance considerations, elucidates these relationships. Useful diagrams derived from this analysis can provide early guidance to aircraft developers in the design process.

Keywords: high-altitude aircraft; solar-electric flight; aircraft design;

1. Introduction to Solar-Electric High-Altitude Aircraft

The first solar-electric aircraft, named Sunrise I, completed its maiden flight on November 4, 1974 [1]. Even then, the idea was to develop an aircraft capable of flying for extended periods at high altitudes above weather phenomena. However, at that time, suitable energy storage options, especially for flying through the night, were not readily available. In 1995, NASA achieved invasion into the stratosphere with the Pathfinder, reaching an altitude of 50,500 feet [2]. On August 13, 2003, the Pathfinder successor, Helios, set the current altitude record for propeller-driven aircraft at 96,863 feet [3]. In 2008, the company QinetiQ accomplished a multi-day flight lasting 82 hours with the Zephyr 6. Finally, on August 19, 2022, a record was set with the Zephyr 8/S for non-refuelable aircraft, surpassing 64 days of flight duration, narrowly missing the overall aircraft endurance record [4]. This progression demonstrates the advancing maturity of solar-electric high-altitude aircraft and could mark the beginning of a novel technology with numerous applications. A typical design of such aircraft, currently under development by the German Aerospace Center, is shown in Figure 1.



Figure 1 – Typical solar-electric high-altitude aircraft

The application areas of solar-electric high-altitude aircraft are particularly in the provision of telecommunications services and Earth observation. In remote areas, such aircraft can implement flying telecommunications towers, eliminating the need for costly ground-based infrastructure. Earth observation tasks can be realized through a variety of sensors. Optical sensors can provide high-resolution images in real-time in the visible light range from high altitudes [5]. Infrared sensors can be deployed at night to identify traffic or individuals. High-flying radar sensors can also detect structures and movements on the ground, even when the line of sight is obscured by clouds [6].

However, the implementation of solar-electric high-altitude aircraft is a challenging engineering task. Figure 2 provides a comprehensive overview of environmental conditions. Below the tropopause, most weather events occur, leading to regular cloud formation and turbulence. Due to the associated shading of the sun and the high structural loads on lightweight structures, a flight altitude below the tropopause is not suitable for extended missions. In the tropopause and slightly above, at altitudes ranging from 30,000 ft to 35,000 ft, the majority of civilian commercial air traffic occurs. Additionally, operations at altitudes up to 60,000 ft might conflict with military air traffic and should generally be avoided due to the significantly different flight speeds of jet-powered transport aircraft and solarelectric high-altitude aircraft optimized for extremely slow flight. Furthermore, operating at these altitudes would occur in controlled airspace (Class C), requiring coordination and cooperative participation in air traffic. Additionally, the certification requirements for operations in Class C airspace are very high. Another disadvantage is the relatively high wind speed at the tropopause level. As shown in Figure 2, with increasing altitude and decreasing air density, flight speed increases at a constant lift coefficient, and wind speed typically decreases above the tropopause. The shown wind curve is an average profile for Hamburg/Germany during spring time. Therefore, it is also reasonable to fly at higher altitudes to reliably station the aircraft over specific locations. To achieve sufficient aerodynamic lift, which requires adequate air density, and having relatively low wind speeds compared to the true airspeed of the aircraft, flight altitudes just above controlled airspace, i.e., just above 60,000 ft, are targeted.

To fly consistently above 60,000 ft, aircraft must be designed with very low power consumption, as the solar radiation power is physically limited. The fundamental operating principle of solar-electric aircraft is illustrated in Figure 3. The only available energy source for sustained flight is the sun. The

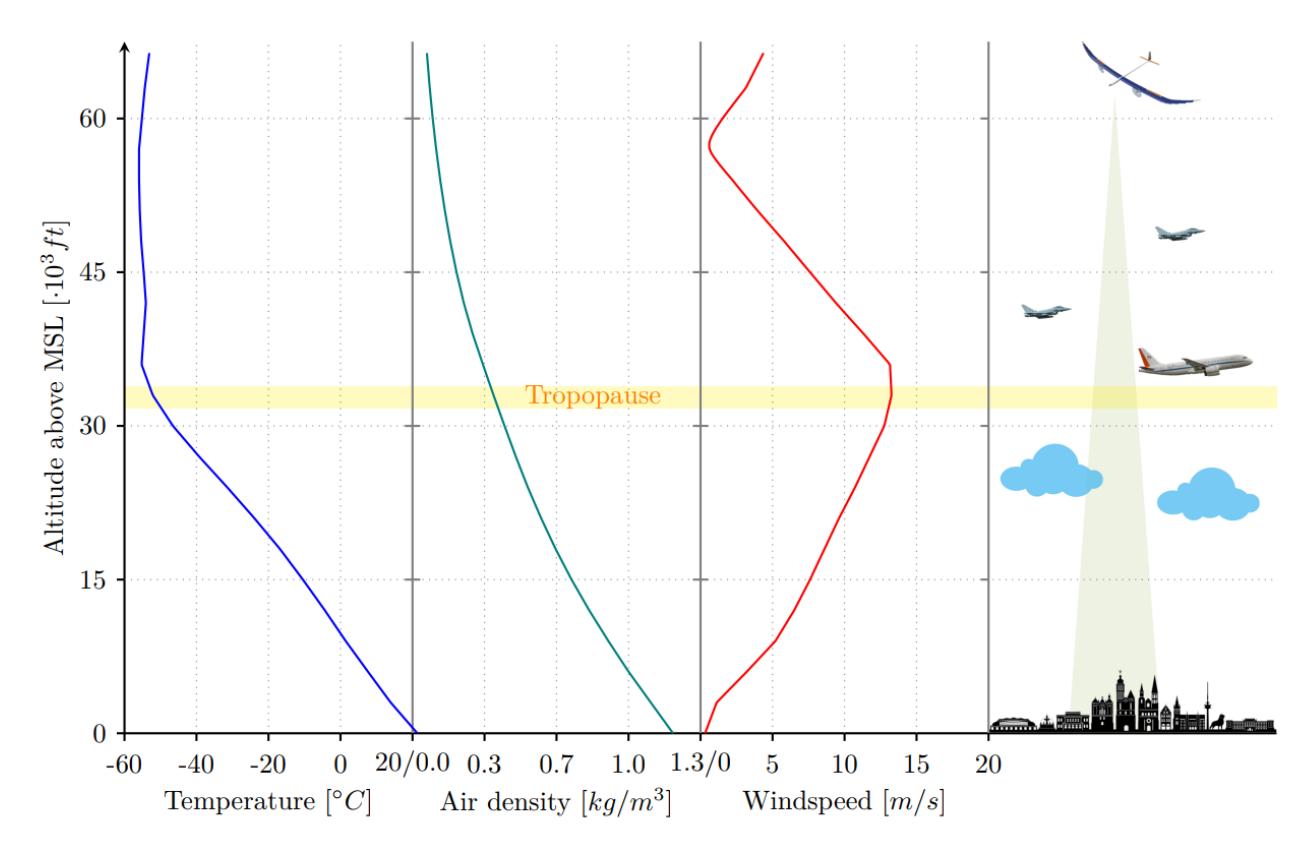


Figure 2 – Overview about the environmental conditions for high-altitude solar-electric flight

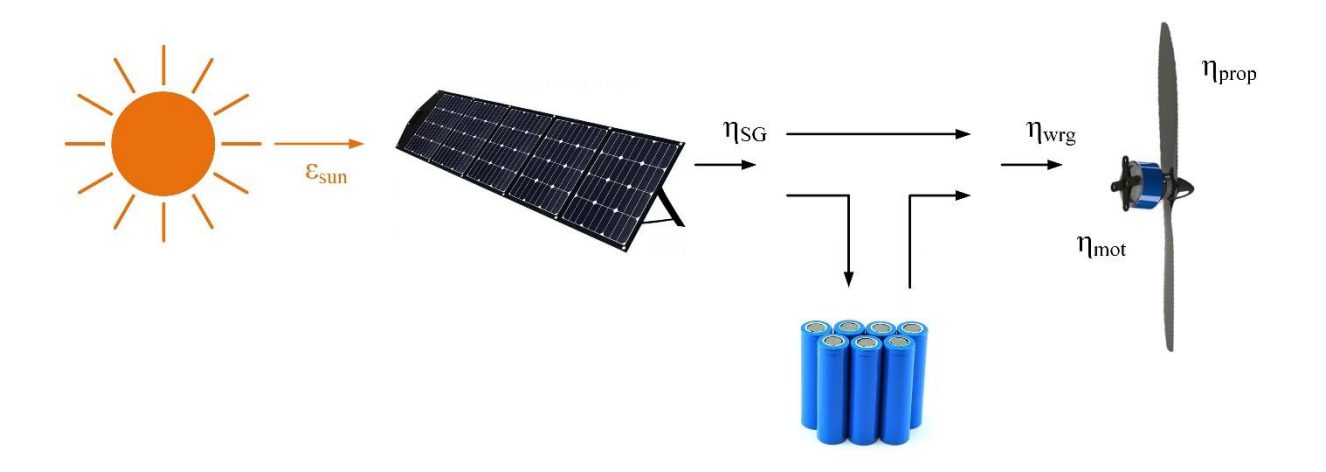


Figure 3 – Basic operation principle of solar-electric aircraft

solar radiation power ϵ_{sun} is converted into electrical power using the photovoltaic cells of the solar generator, depending on their efficiency η_{SG} . The electrical power is then directly used for the propulsion of the aircraft, considering losses in the electrical lines through the efficiency η_{wrg} , as well as the efficiencies of the electric motor and the propeller through η_{mot} and η_{prop} . Excess power is stored in batteries to supply the aircraft with electrical power during nighttime when little to no solar radiation power is available.

In the following sections, fundamental design relationships for achieving this are discussed. Chapter 2 begins by describing the modeling of environmental conditions with a specific focus on solar radiation from the sun. Chapter 3 provides an analytical description of the essential system components and the flight performance of the aircraft. Chapter 4 integrates environmental models and flight performance descriptions into an energy analysis. Based on this, feasibility diagrams concerning design-relevant parameters are created and discussed. The publication concludes with a summary and an outlook.

2. Modelling the Environment

2.1 Solar Radiation

The sun is the sole source of energy for sustained flight. Since the solar radiation power is not constant but rather dependent on the daily cycle, a model is necessary to determine the available solar power. In Figure 4, the spectrum of solar radiation is provided for various path lengths of sunlight through the atmosphere. Airmass (AM) 0 refers to the radiation intensity outside the atmosphere. AM 1 represents the spectrum at the Earth's surface when the sun is at zenith, and AM 1.5 is particularly relevant for mid-latitudes, as it is considered a kind of standard value, representing the spectrum at the Earth's surface for a solar elevation of ζ_{sun} =48°.

The area-specific direct radiation power density ϵ_{dir} can be determined by integrating over the spectrum, which can be calculated, for example, using the NREL SMARTS [7] model:

$$\varepsilon_{\rm dir} = \int_0^\infty \varepsilon_\lambda \cdot d\lambda \tag{1}$$

For the design of solar-electric aircraft, it is particularly interesting to know how much energy is available over a day/night cycle. For this purpose, it is first necessary to calculate the suns position. The relevant rotation sequences for this are illustrated in Figure 5. The aircraft is located at the

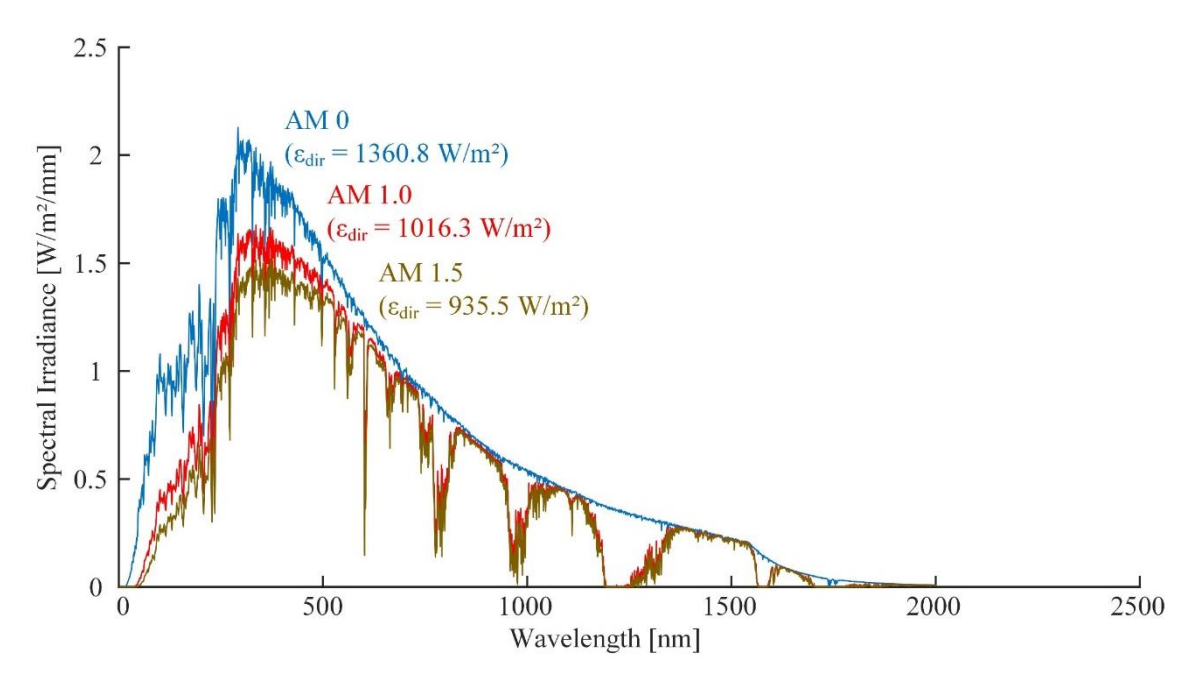


Figure 4 – Solar spectrum for different air masses

geographic longitude λ and geographic latitude ϕ . Depending on the day of the year d, the axial tilt of the Earth δ_E towards the sun is initially determined:

$$\delta_E = -23.5^o \cdot \cos \frac{2 \cdot \pi}{65} \cdot (d+10) \tag{2}$$

For the solar hour angle, the following equation holds, where td is the time of the day in seconds:

$$\tau_E = \frac{\pi}{43.200s} \cdot t_d \tag{3}$$

The solar zenith angle ζ_{sun} , illustrated in Figure 5, is the angle between the normal vector of the tangential surface at the point of reception of the sunbeam and the sunbeam itself. The solar zenith angle is calculated by:

$$\sin \zeta_{sun} = \sin \lambda \sin \delta_E + \cos \lambda \cos \delta_E \cos(\phi + \tau_E)$$
 (4)

With the help of the zenith angle, the radiation component perpendicular to the receiver surface can now be calculated:

$$\varepsilon_{normal} = \varepsilon_{dir} \cdot \cos(\zeta_{sun}) \tag{5}$$

Due to its dependence on the solar position and, therefore, the path length through the atmosphere, the radiation power density is time-dependent. To determine the available energy per area and day/night cycle, the direct radiation power density must be temporally integrated over the cycle duration:

$$e_{dir} = \int_0^{24h} \varepsilon_{dir} \cdot dt \tag{6}$$

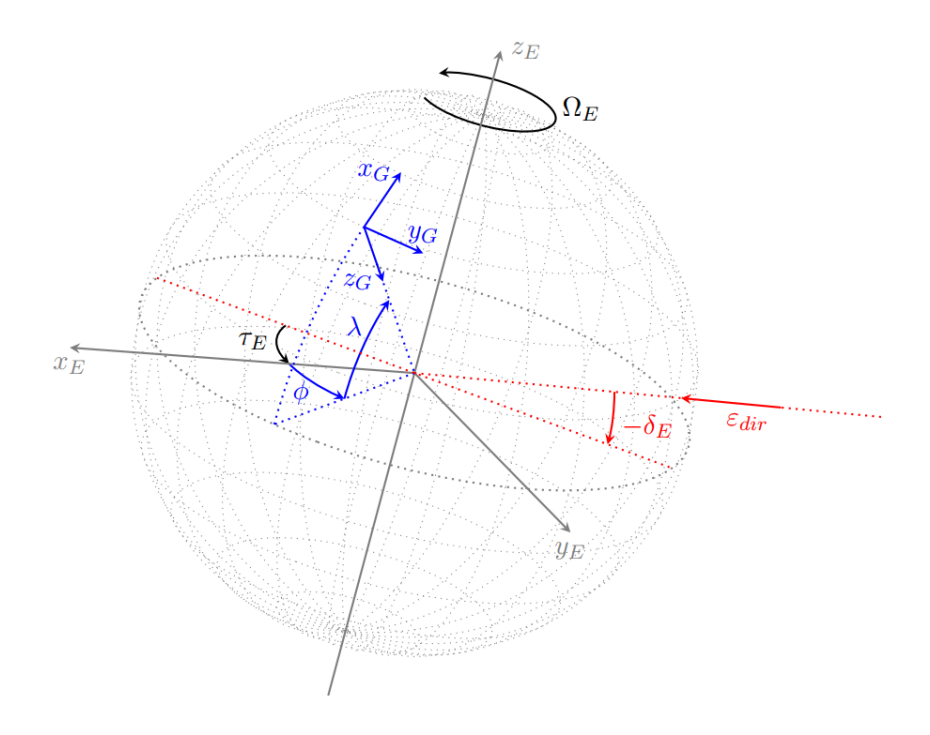


Figure 5 – Solar radiation relevant angles

The calculation for the radiation component to a horizontal receiver surface follows in a similar manner. It is now possible to represent the available energy density over the year and for the geographical latitudes of a hemisphere. In Figure 6, the energy density, assuming that the receiver surface is continually perpendicular to solar radiation, is depicted for an altitude of 60,000 ft. To achieve this ideal state, continuous tracking of the receiver surface would be necessary. In the case of a horizontal receiver surface, the results are presented in Figure 7.

It is evident that, assuming continuous perpendicular irradiation of the receiver surface, significantly higher energy yields throughout the day can be achieved, especially in high northern latitudes. If the receiver surface is not tracked, which is approximately the case when photovoltaic cells are applied on the wing surface, the yield is lower on one hand, but also somewhat more uniform throughout the entire year, which is favorable for designing the system to operate over a complete year. From Figure 7, it follows that for year-round operation in latitudes up to 20°, approximately 8 kWh/m² is available.

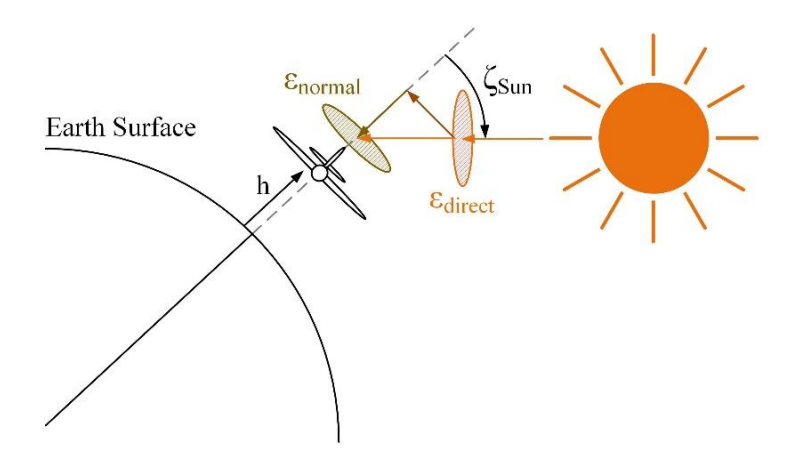


Figure 6 - Solar radiation incidence on aircraft wing

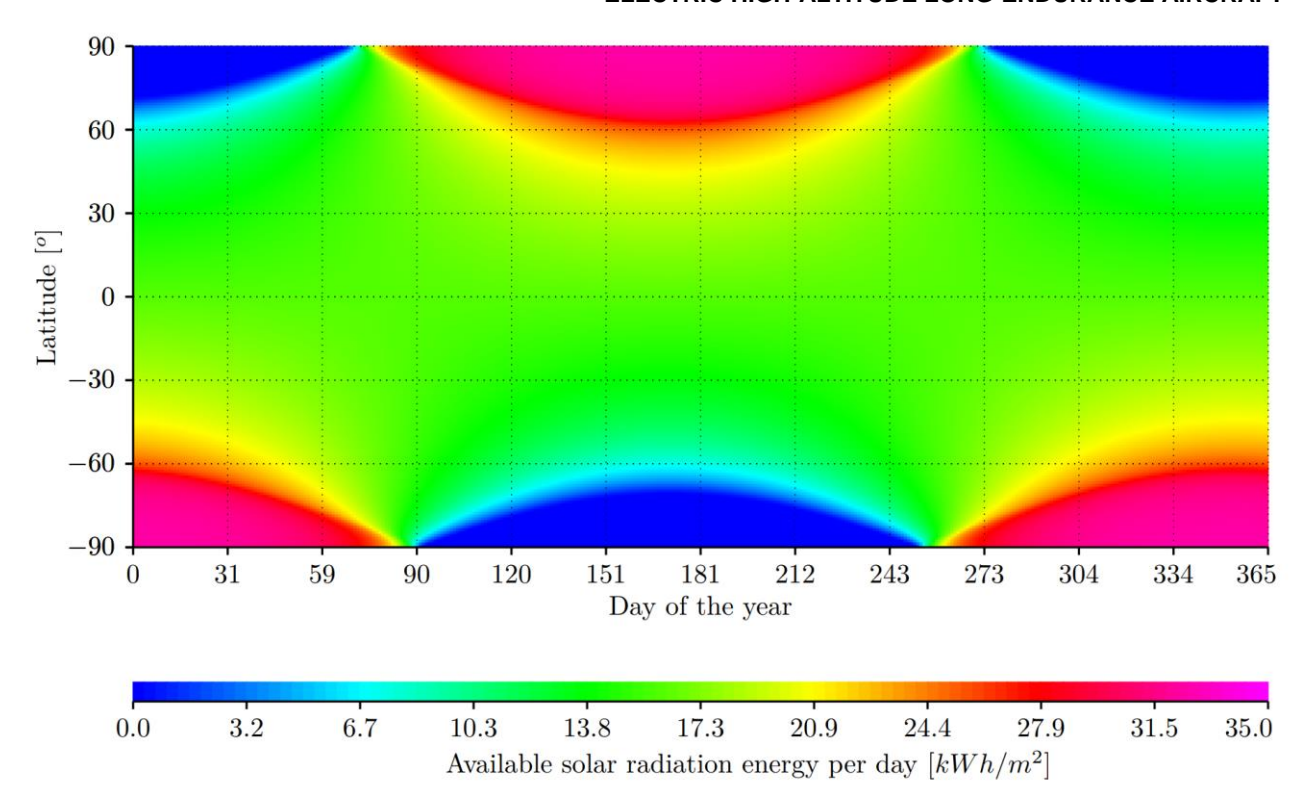


Figure 7 – Energy density of solar direct radiation

As expected, in the summer months and at latitudes further north, more energy per day/night cycle is available. However, depending on the design of the aircraft, year-round operation may not be feasible in those regions.

Finally, it should be noted that the analysis considered only the direct component of solar radiation. At sea level, scattered radiation plays a significant role alongside direct radiation, but at altitudes of 60,000 ft, its contribution is sufficiently low to justify neglecting it in the analysis.

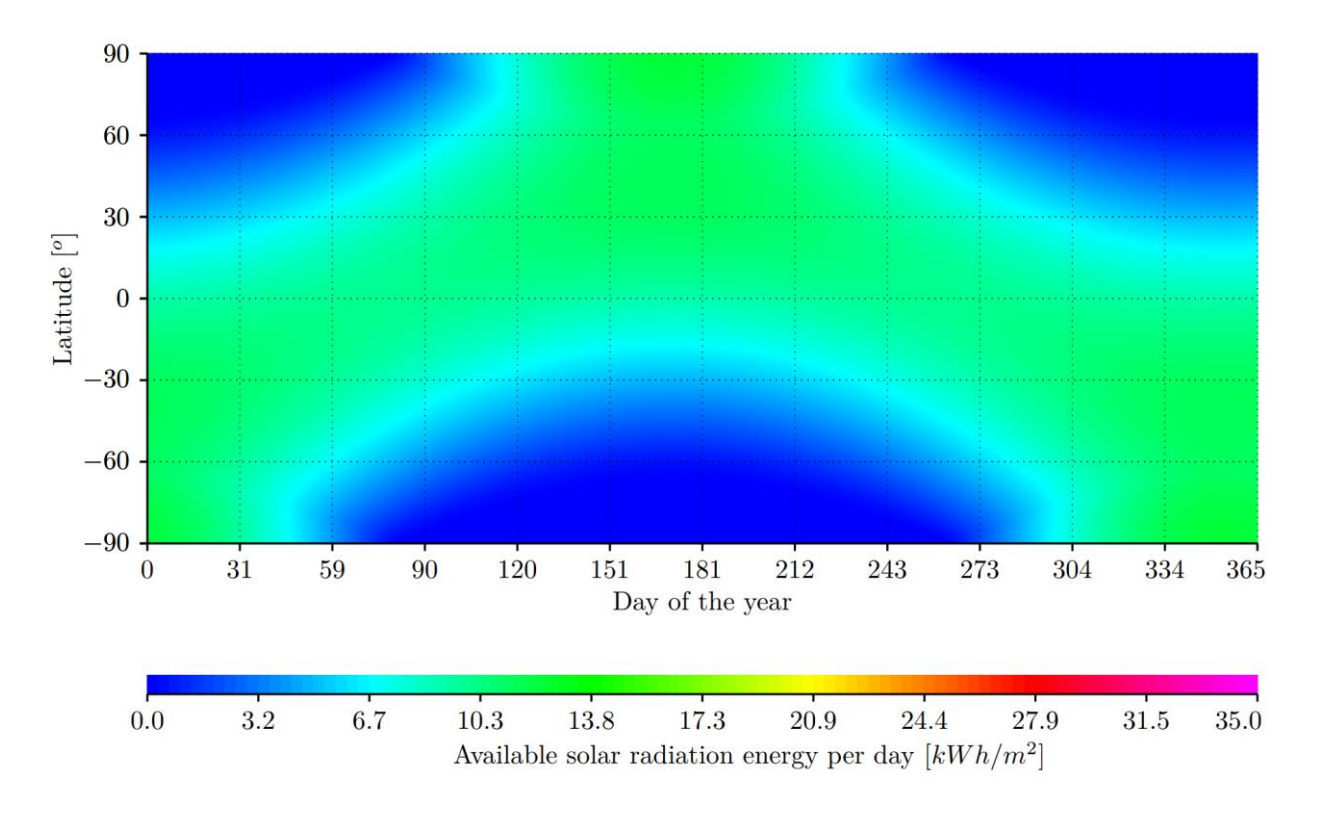


Figure 8 – Energy density of solar normal radiation

2.2 Atmosphere

For the considerations in this work, the NASA Standard Atmosphere of 1976 [8] is applied. Although the values contained therein may not precisely match local conditions, they are sufficiently suitable for the analyses within the scope of this publication. The density profile is significant since this value scales the true airspeed within the atmosphere and plays an important role in the subsequent discussions. At sea level, according to the NASA Standard Atmosphere, the air density is:

$$\varrho(h = 0 \text{ ft}) = 1.225 \frac{kg}{m^3} \tag{7}$$

At an altitude of h = 60.000 ft, the air density is:

$$\varrho(h = 60,000 \text{ ft}) = 0.088 \frac{kg}{m^3} \tag{8}$$

Additional atmospheric data are not utilized for the further analyses. For further investigations, it is also worth considering the use of more powerful atmospheric models. On one hand, the density distribution changes with altitude as latitude varies, and on the other hand, more realistic temperature values are provided. In this regard, the NASA Global Reference Atmospheric Model [9] is a suitable option, for example.

3. Aircraft Systems and Flight Performance

3.1 Solar System

The solar radiation from the sun is converted into a free electron current by photovoltaic cells, with the photovoltaic cell acting as a current source. The conversion undergoes a wavelength-dependent efficiency, which is typically greater than 0 only for a portion of the spectrum. Due to the spectral attenuation of solar radiation, the efficiency of photovoltaic cells is dependent on the air mass (AM) through which it travels. However, at 60.000 ft altitude, the attenuation of the solar spectrum is sufficiently low to justify assuming the extraterrestrial efficiency for the chosen photovoltaic cell. Therefore, all further information relates to efficiencies outside the atmosphere unless otherwise stated.

Various technologies for photovoltaic cells are considered for solar-electric aircraft. Figure 9 provides an overview of the development of the conversion efficiency of various solar cell technologies. Although these are laboratory measurements, it is noteworthy that many technologies have gained a significant efficiency improvement in the past 10 years. Silicon solar cells are widespread, achieving efficiencies of up to 22% on a module level in monocrystalline form. For example, the NASA Helios was equipped with this technology. The drawback of silicon technology is its high weight, given by the relatively thick cells and required lamination to make them sufficiently flexible. Currently, weights of approximately 700 g/m² can be achieved.

Cadmium Indium Gallium Selenide (CIGS) thin-film photovoltaic cells are manufactured directly on foils using a roll-to-roll process, and at the cell level, they are characterized by flexibility and a very low weight of less than 100 g/m². Moreover, efficiencies of 20% on a module level are possible here as well. However, the cells' resistance to moisture and oxygen is a significant problem, which is practically solved by laminating them in thick hermetically sealed foils, resulting in module-level weights of over 600 g/m².

Currently, photovoltaic cells based on Gallium Arsenide are used for solar-electric high-altitude aircraft. Single-junction cells achieve efficiencies of up to 24% on a module level, while tandem cells with three different cell materials can achieve up to 30% efficiency. Weights of 330 g/m² are achievable on a module level. For example, the Zephyr 8/S uses tandem photovoltaic cells from the manufacturer MicroLink Devices [10].

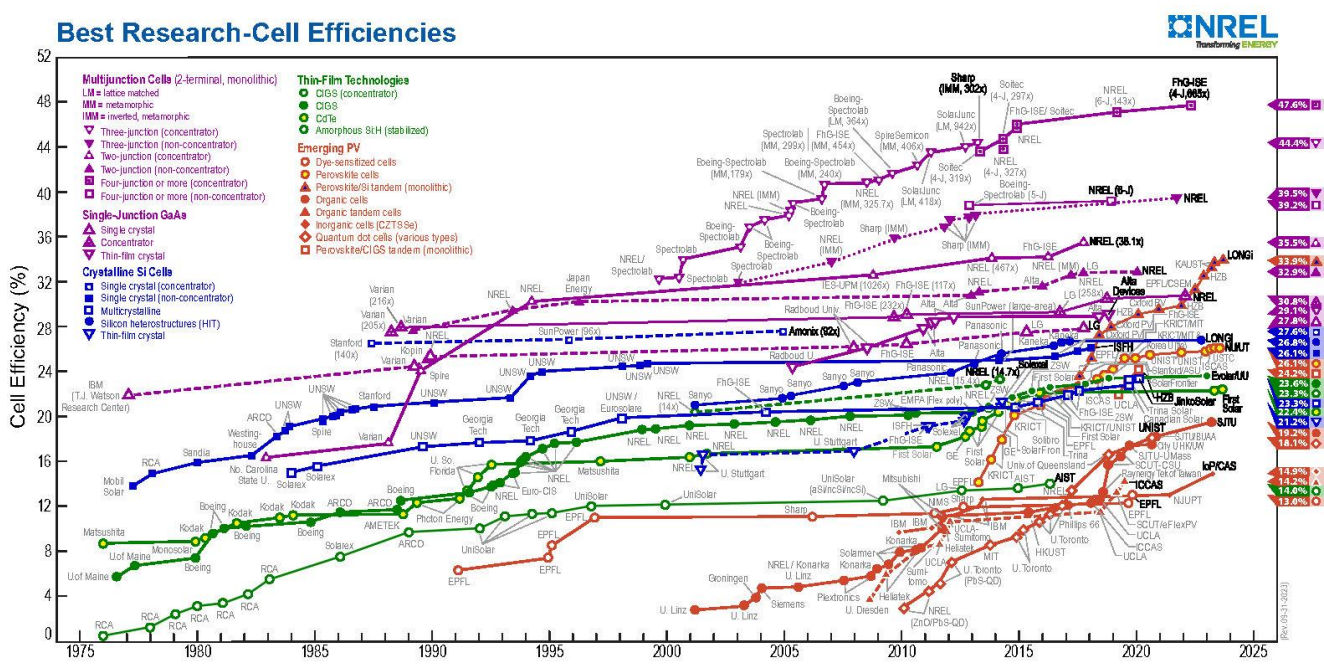


Figure 9 – NREL chart about the progress of solar cell efficiency for different technologies (Source: [11])

Photovoltaic cells are radiation-dependent power sources. The power output is determined by the voltage applied to the cell. Optimal operation is achieved when using Maximum Power Point Trackers (MPPT), which track the voltage across the cells in such a way that they deliver their maximum electrical power. Additionally, MPPTs act as impedance converters with respect to the receiving network. In the following, the use of MPPTs is assumed. Trade studies regarding their use may still be meaningful at a later time since optimizing energy yield comes at the expense of the additional weight of these devices. Using MPPTs, it can be assumed that the solar cells are continuously operated at maximum efficiency. Furthermore, in the context of this publication, it is assumed that the photovoltaic cells are mounted on the upper side of the wing, which is covered with the covering factor κ . Additionally, it is simplistically assumed that the upper surface of the wing is sufficiently parallel to the tangent at the Earth's surface. It follows:

$$p_{el,SG} = \kappa \cdot \eta_{SG} \cdot \varepsilon_{normal} \tag{9}$$

Similarly, the electrical energy yield can be calculated by:

$$e_{el,SG} = \kappa \cdot \eta_{SG} \cdot e_{normal} \tag{10}$$

Assuming an efficiency of 28%, according to Figure 7, it follows that only 2.3 kW/m² is available for the day with the lowest solar yield, assuming year-round flight at 20° northern latitude.

3.2 Battery System

In the field of batteries, there has been a dynamic development in recent years. In comparison to lightweight, flexible, and highly efficient photovoltaic cells, the automotive industry, in particular, has driven progress, providing a mass complementary market.

In addition to the widespread lithium-ion (Li-Ion) batteries with lithium cobalt dioxide (LiCoO2) cathodes, alternative technologies have now reached higher levels of maturity. Achieving high gravimetric energy densities, cycle durability, and safety against battery fires are essential criteria, especially given the mass adoption in the automotive industry.

Figure 10 (based on data from [12]) provides an overview of the gravimetric and volumetric energy density of various technologies for lithium-based battery cells. Lead-acid batteries, as well as nickel-cadmium (Ni-Cd) and nickel-metal hydride (Ni-MH) batteries, are included for comparison purposes

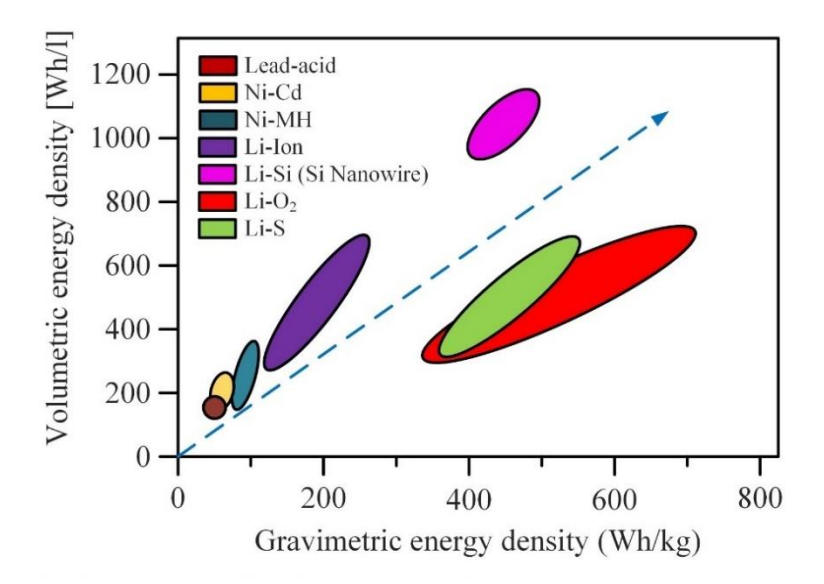


Figure 10 - Gravimetric and volumetric energy densities for different battery cell technologies

and are not suitable for high-flying solar aircraft due to their low energy density. Classical Li-lon batteries currently achieve energy densities of up to 300 Wh/kg at very low costs. Lithium-sulfur (Li-S) batteries were once considered a promising option for increasing battery energy density; however, challenges such as cycle durability and fire protection still needed to be addressed.

Lithium-air (Li-O2) batteries are currently still under research but are listed here as a representative of potential future technologies. Promising are lithium batteries with a silicon anode (Li-Si). In these batteries, microcracks quickly appeared due to the charge-dependent volume of silicon, leading to low cycle stability. The use of silicon in the form of nanowires seems to significantly address this issue. Due to its now achieved maturity, this technology is currently being used in the Zephyr 8/S [13] and other high-altitude solar aircraft. On a cell level, an energy density of up to 500 Wh/kg can be assumed, with degradation of this value at the battery system level, accounting for wiring, battery management systems, thermal insulation, and conditioning, to be around 350 Wh/kg.

The availability of rechargeable batteries with the mentioned energy densities has led to the current situation where no project for the realization of a long-endurance high-altitude solar aircraft is known to rely on alternative technologies, such as fuel cell systems with electrolyzers.

3.3 Propulsion System

The propulsion of solar-electric high-altitude aircraft is typically achieved through propellers. It is important to consider whether fixed-pitch or variable-pitch propellers should be used. Opting for a fixed-pitch propeller that is optimized for operation at high altitudes may result in very large torques and low speeds during ascent at low altitudes. The electric drives must be able to deliver these torques without overheating during the climb. Variable-pitch propellers can mitigate this problem but are more complex in structure and have higher weight.

For the considerations in this publication, only level flight is examined, assuming that the propeller is optimized for the operational altitude. In Figure 11, the efficiency of a propeller is exemplarily shown as a function of the advance ratio. The advance ratio is the ratio of free-stream velocity, i.e., the true velocity in the atmosphere, to the blade tip speed of the propeller. It is evident that at a similar advance ratio, the propeller's rotational speed must also increase with altitude.

Very good propellers can achieve efficiencies of up to $\eta_{prop} = 0.8$. Since a consistent optimization for high-altitude flight cannot be assumed due to the climb through the lower atmosphere, the following calculations use a propeller efficiency of $\eta_{prop} = 0.7$.

Furthermore, the electric drive motor must be considered. Typically, this is implemented as a permanent magnet synchronous machine and controlled by an inverter, also known as a motor controller. Modern MOSFET-based power electronics can achieve efficiencies of up to 98% for the motor controller. The motors themselves have efficiencies well above 90% at their optimal operating points. For a realistic estimation, a total efficiency of $\eta_{mot} = 0.9$ is assumed in the following calculations.

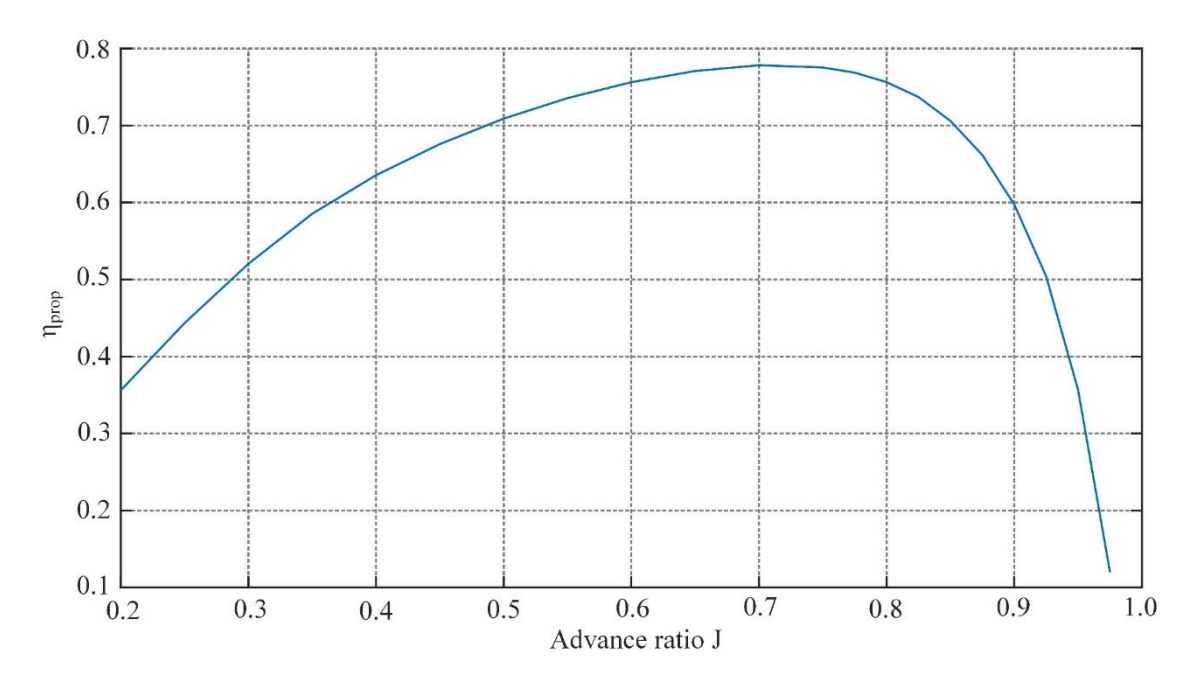


Figure 11 – Propeller Efficiency in dependency of the advance ratio

3.4 Flight Performance

To estimate the flight performance, first a look at the wing profiles is taken. Due to the high altitude and the energy-optimized slow flight, it is necessary to choose a profile that provides sufficiently low drag and sufficiently high lift coefficients at low Reynolds numbers. The Reynolds number is defined as:

$$Re = \frac{\varrho \cdot V_{TAS} \cdot L}{n} \tag{11}$$

Here, η is the dynamic viscosity, and L is the characteristic length. For a wing profile with a 1.4 m cord length, the Reynolds number at a flight altitude of 60,000 ft is 270,000.

Due to the finite stiffness of the wing, there are local deformations that result in different lift coefficients at different locations on the wing. Furthermore, the lift coefficient decreases toward the wingtips. Therefore, the aircraft cannot achieve the maximum possible lift coefficient of the profile. For further calculations, based on Figure 12, which shows a typical profile for low Reynolds numbers, we assume a maximum achievable lift coefficient for the aircraft of $C_L = 1.1$.

The forces acting on the aircraft are shown in Figure 13. For the lift force L, which must compensate for the weight, we have:

$$L = m_{ac} \cdot g = \frac{\varrho}{2} \cdot V_{TAS}^2 \cdot C_L \cdot S_{ref}$$
 (12)

Here, S_{ref} represents the reference area, which, in the following considerations, corresponds to the area of the wing. The thrust T must compensate for the drag D. The drag is given by:

$$D = T = \frac{\varrho}{2} \cdot V_{TAS}^2 \cdot C_D \cdot S_{ref} \tag{13}$$

The propeller's power is proportional to thrust and flight speed, which leads to:

$$P_{prop} = T \cdot V_{TAS} \tag{14}$$

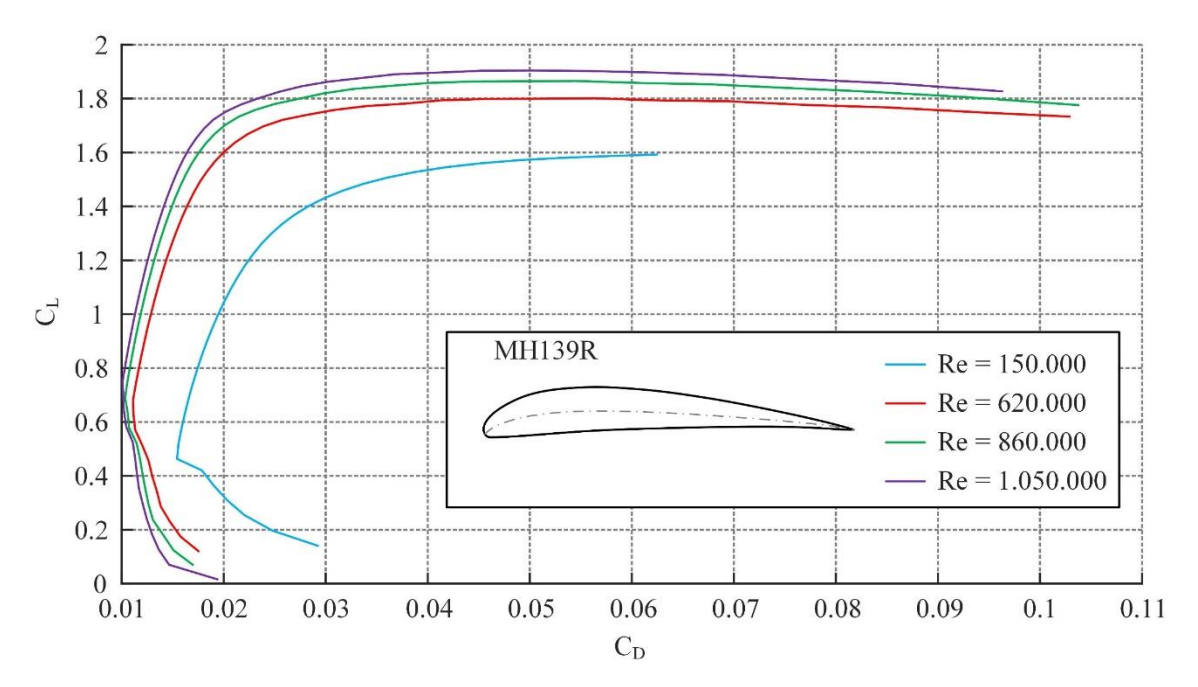


Figure 12 - Example of a low speed low Re airfoil

With the efficiency of the motor, propeller, and electrical lines, the electric propulsion power is given by:

$$P_{prop,el} = \frac{1}{\eta_{mot} \cdot \eta_{wrg} \cdot \eta_{prop}} \cdot P_{prop}$$
 (15)

The total drag is assumed, based on an elliptical drag polar, to be:

$$C_D = C_{D0} + \frac{C_L^2}{\pi \Lambda e} \tag{16}$$

Here, Λ represents the aspect ratio, and e is the Oswald factor, which measures the wing's shape efficiency, i.e., how well the lift distribution resembles the optimal elliptical distribution. A value of 0.9 is assumed for the Oswald factor in the following analyses.

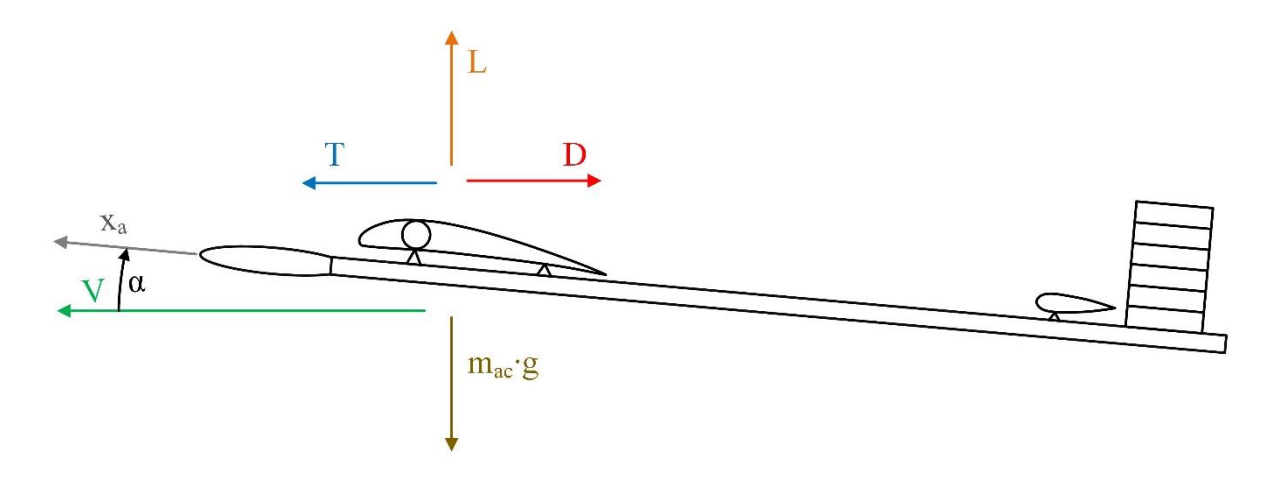


Figure 13 - Force at the aircraft in steady state flight

Substituting these formulas and relating the electric propulsion power to the reference area, we get the so-called power loading:

$$p_{el,prop} = \frac{P_{el,prop}}{S_{ref}} = \frac{1}{\eta_{mot} \cdot \eta_{wrg} \cdot \eta_{prop}} \cdot \sqrt{\frac{2}{\varrho} \cdot \left(\frac{m_{ac}}{S_{ref}}\right)^{\frac{3}{2}}} \cdot g^{\frac{3}{2}} \cdot \left(\frac{C_{D0}}{\frac{3}{C_L^2}} + \frac{1}{\sqrt{C_L}\pi\Lambda e}\right)$$
(17)

The wing loading is included as:

$$W_L = \frac{m_{ac}}{S_{ref}} \tag{18}$$

Now, let's consider the electric power provided by the photovoltaic cells. For this, we first calculate the power loading for an aircraft with the following parameters, shown in Table 1. The relevant results are shown in Figure 14, where the red line represents the power consumption and the blue line the generated power.

| Parameter | Value | Parameter | Value |
|-----------------|-----------------------|-------------------|-------|
| WL | 3.7 kg/m ² | К | 0.7 |
| CL | 1.1 | ηsg | 0.28 |
| C _{D0} | 0.02 | η _{mot} | 0.9 |
| ٨ | 21 | η _{prop} | 0.7 |
| е | 0.9 | η _{wrg} | 0.9 |

Table 1 - Parameters of example aircraft

The blue area represents the energy surplus during the day, while the red area represents the storage capacity of the batteries. The transition region between day and night is noticeable, during which the aircraft is partly supplied from batteries and partly from the solar generator. In the shown case, there

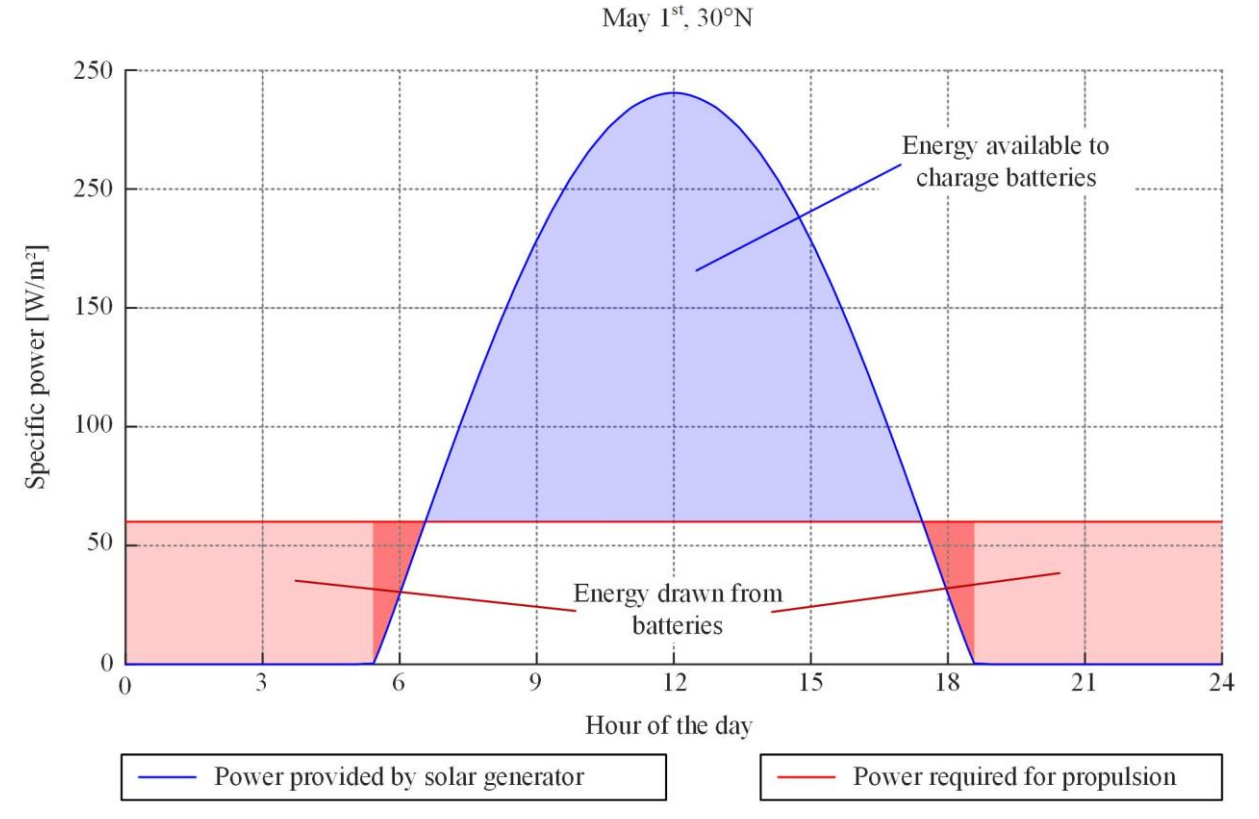


Figure 14 - Example of a specific power chart

would be sufficient solar energy available to fly the day/night cycle with the aircraft, as the red area is smaller than the green area. Using Figure 8, it can be estimated whether enough energy is provided by the sun for a 24-hour flight. The calculated power loading is $p_{el,prop} = 58W/m^2$. The energy requirement is obtained by multiplying with 24 hours, dividing by the coverage factor κ , and the efficiency of the photovoltaic cells, resulting in 7,1 kWh/m², which is lower than the available value of 10.2 kWh/m². Now, the storage requirement of the battery needs to be determined, for which the red area is calculated as follows:

$$e_{bat} = \int_0^{24h} \Delta p_{pos}(t) dt \tag{19}$$

Where the integrand is the positive value of the difference between the power loading and the provided specific power of the solar generator:

$$\Delta p_{pos} = \begin{cases} p_{el,prop} - p_{el,SG} \mid p_{el,prop} - p_{el,SG} > 0 \\ 0 \mid otherwise \end{cases}$$
 (20)

The now available energy density per wing area can finally be converted into a gravimetric energy density. However, a mass fraction of the battery to the total aircraft must be assumed. For solar-electric high-altitude aircraft, this fraction lies in the area of up to 50%, and in the following calculations. The formula for gravimetric energy density is:

$$e_{bat,gr} = \frac{e_{bat}}{W_L} \cdot \frac{m_{ac}}{m_{bat}} \tag{21}$$

With the provided formulas, it is now possible to estimate fundamental design parameters for desired operational scenarios.

4. Feasibility Analysis

Based on the derived formulas, the design space for solar-electric stratospheric aircraft will now be explored. Equation (17) indicates that the power required for propulsion depends exponentially on the wing loading. First, we will determine the maximum wing loading that allows for a 24-hour flight at an altitude of 60.000 ft with a balanced energy budget. A balanced energy budget means that the energy absorbed for propulsion over 24 hours equals the energy provided by the sun. It is also assumed that the solar panels are mounted horizontally on the wing.

Initially, the average solar power is calculated by integrating Equation (5) analogously to Equation (6) and then dividing by 24 hours. The electrical power provided by the solar panels is determined using Equation (9). This results in:

$$\overline{p_{el,SG}} = \kappa \cdot \eta_{SG} \cdot \frac{1}{24h} \int_0^{24h} \varepsilon_{dir} \cdot \cos(\zeta_{sun}(t)) \cdot dt$$
 (22)

The maximum permissible wing loading can now be determined by substituting Equation (22) into Equation (17) as follows:

$$W_{L,max} = \left(\frac{\overline{p_{el,SG}} \cdot \eta_{mot} \cdot \eta_{wrg} \cdot \eta_{prop}}{\sqrt{\frac{2}{\varrho}} \cdot g^{\frac{3}{2}} \cdot \left(\frac{C_{D0}}{C_L^{\frac{3}{2}}} + \frac{1}{\sqrt{C_L}\pi\Lambda e}\right)}\right)^{\frac{2}{3}}$$
(23)

By retaining the parameters given in Table 1 except for the wing loading, a chart can now be created that indicates the maximum permissible wing loading for the days of the year and latitude. The resulting chart for an altitude of 60,000 ft is shown in Figure 15.

These results are particularly representative of aircraft covered with thin film, such as the Airbus Zephyr 8/S. These types of aircraft can be designed to achieve wing loadings of down to 2.5 kg/m². Typically, a spar-and-rib construction method is chosen, leading to very lightweight constructions, but with relatively low bending stiffness. The wingspan of such aircraft cannot be arbitrarily increased, as the diameter of the spar becomes too small relative to the wingspan due to the decreasing profile thickness with reduced chord depth. Therefore, minimizing energy consumption is achieved by minimizing flight speed.

The limits shown in Figure 15 can be adjusted to some extent by reducing parasitic drag and through other optimization measures, but fundamentally, an extremely lightweight aircraft is required. Given that low wing loadings are particularly problematic in turbulence and flight speeds often match local wind speeds, it is worth considering whether fundamental design adjustments could yield benefits.

If an integral wing is implemented instead of film covering, the significantly higher aerodynamic efficiency can substantially reduce parasitic drag. Additionally, it becomes possible to achieve much higher aspect ratios. In Figure 16, the results for adjusting the aspect ratio to Λ = 40 and reducing parasitic drag to C_{D0} =0.012 are shown. It is evident that the permissible wing loadings can be increased by approximately 50%.

A design that fits this concept is the BAE-developed aircraft PHASA-35 [14]. With a mass of around 150 kg, an estimated wing loading of approximately 5 kg/m² can be achieved, suggesting a flight range that is somewhat more restricted compared to the Zephyr 8, though a year-round operation seems possible. It is noted that the construction concept required for realizing high-aspect-ratio solar-electric high-altitude aircraft entails an increase in structural mass, necessitating a careful trade-off between concepts during the design phase. The higher flight speed resulting from increased wing loading is advantageous for countering local winds and enhances the aircraft's robustness against wind shear during ascent and descent.

After addressing the question of maximum wing loadings, the energy requirement for overnight flight must be determined to estimate battery capacity. Using Equation (19), the storage requirement for a fixed wing loading is calculated. To be independent of assumptions regarding the battery's mass fraction of the aircraft's total mass, the resulting energy density is initially related to the aircraft mass. Thus, the aircraft can be considered as a flying battery with a required gravimetric energy density. For

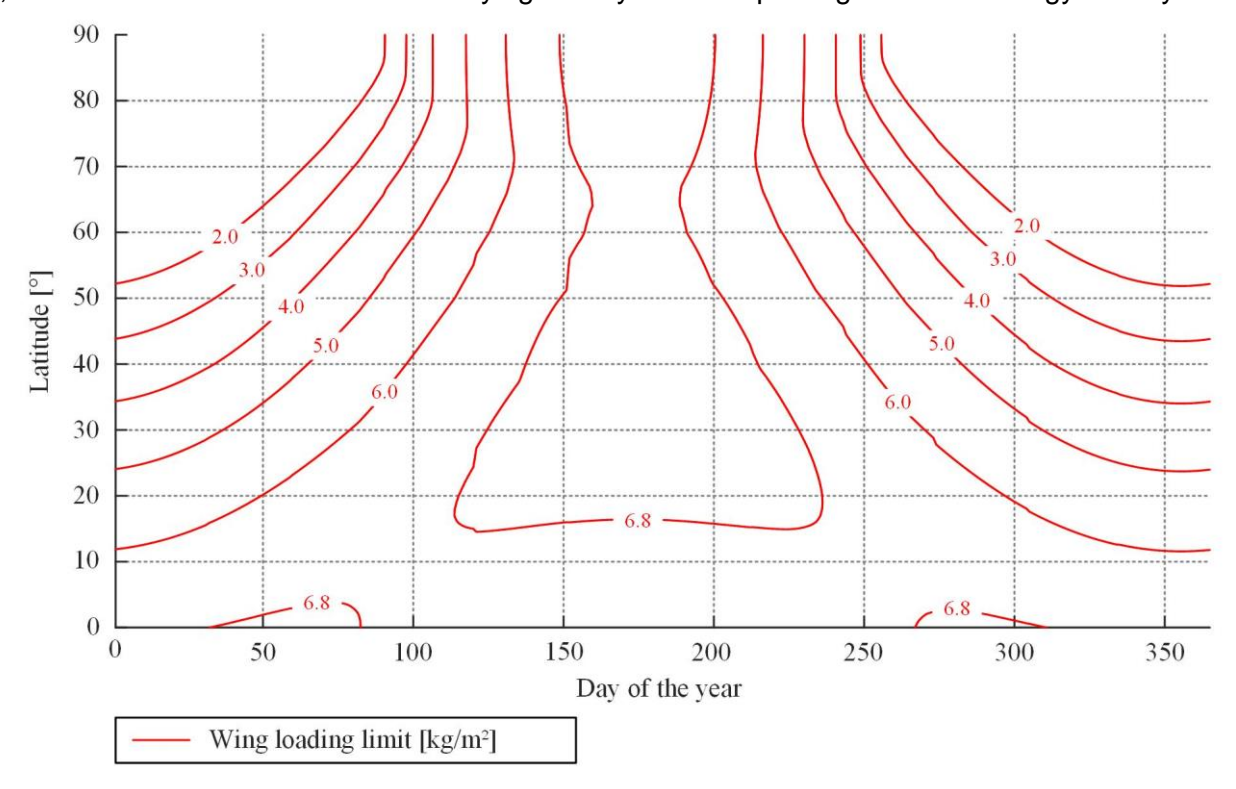


Figure 15 – Maximum wing loading chart for C_L = 1.1, C_{D0} = 0.012, Λ =40, e= 0.9, κ =0.7, η_{SG} =0.28, η_{mot} =0.9, η_{prop} =0.7, η_{wrg} =0.9

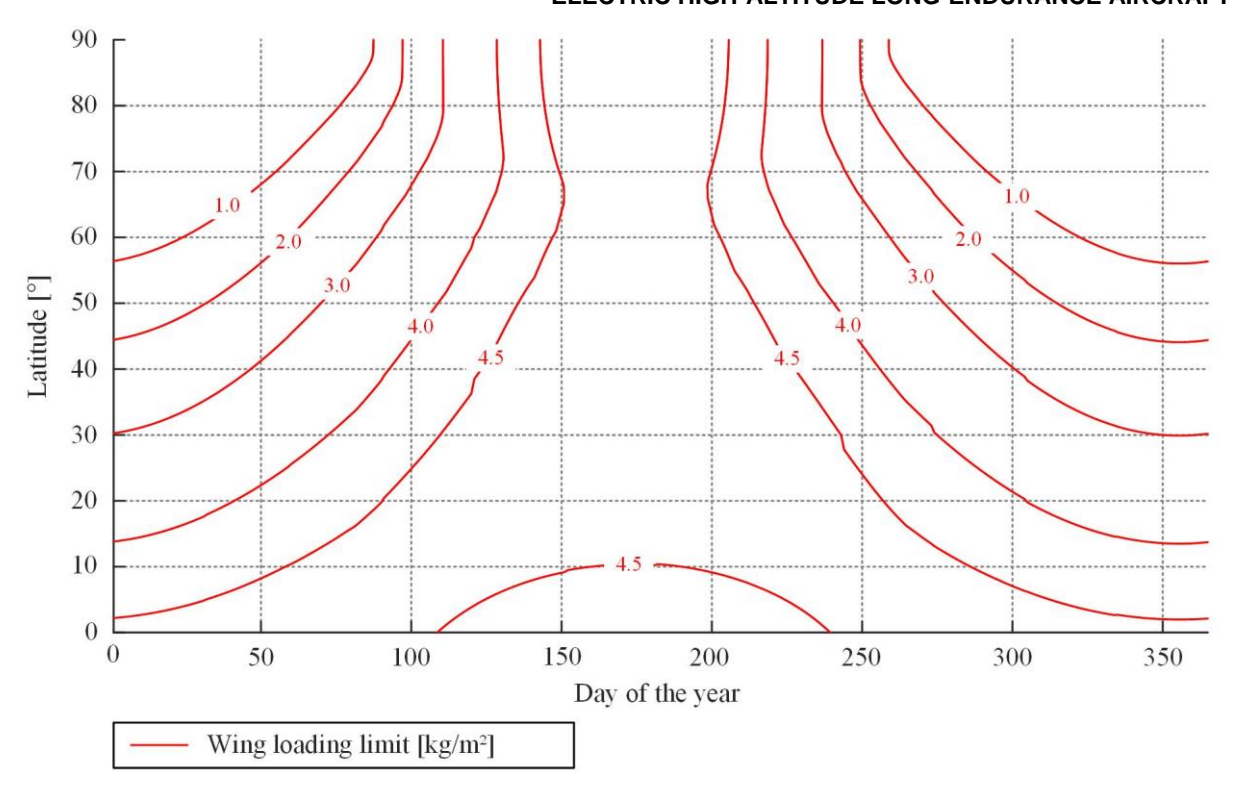


Figure 16 – Maximum wing loading chart for CL = 1.1, CD0 = 0.02, Λ =21, e= 0.9, κ =0.7, η_{SG} =0.28, η_{mot} =0.9, η_{prop} =0.7, η_{wrg} =0.9

low aspect ratios, the results are shown in Figure 17. To utilize the full flight range, an energy density of approximately 180 Wh/kg is required. Assuming that batteries with a usable energy density of about 400 Wh/kg are available, it is clear that around 45% of the aircraft's total mass must be allocated for batteries. Considering the low wing loadings, this poses particular challenges for aircraft design, as the available surface-related mass for structure and systems is reduced to less than 1.5 kg/m².

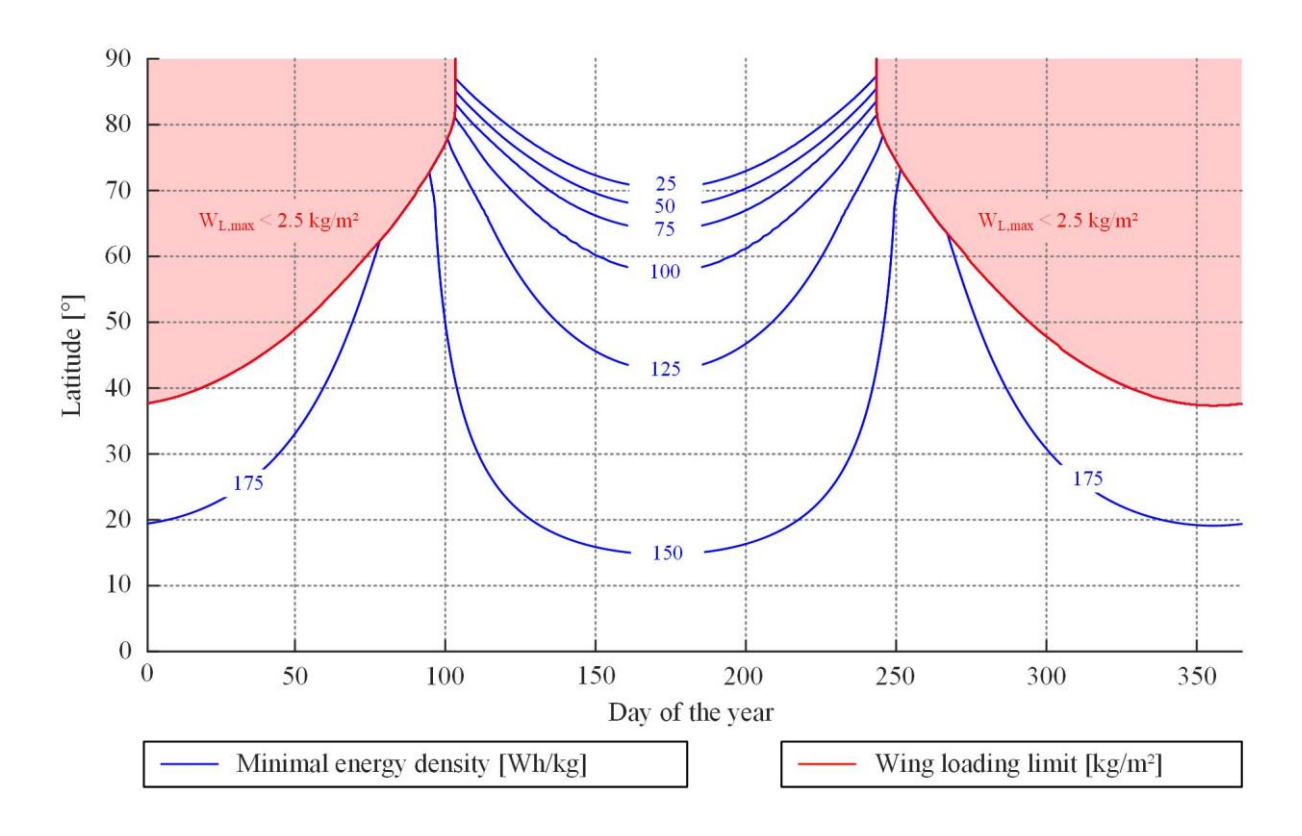


Figure 17 – Required energy density to store electrical energy for the overnight flight phase for $W_L = 2.5 kg/m^2$, $C_L = 1.1$, $C_{D0} = 0.02$, $\Lambda = 21$, e = 0.9, $\kappa = 0.7$, $\eta_{SG} = 0.28$, $\eta_{mot} = 0.9$, $\eta_{prop} = 0.7$, $\eta_{wrg} = 0.9$

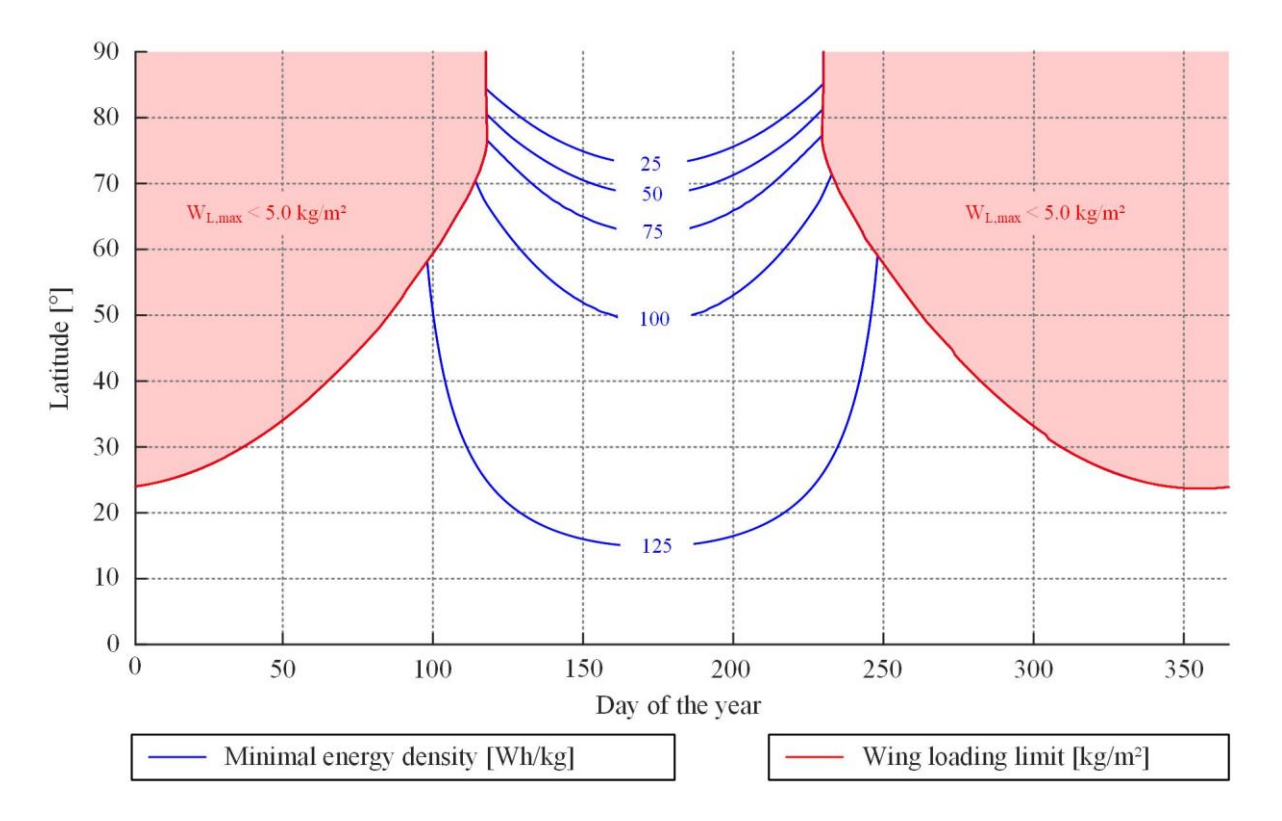


Figure 18 – Required energy density to store electrical energy for the overnight flight phase for $W_L = 5.0 \text{kg/m}^2$, $C_L = 1.1$, $C_{D0} = 0.012$, $\Lambda = 40$, e = 0.9, $\kappa = 0.7$, $\eta_{SG} = 0.28$, $\eta_{mot} = 0.9$, $\eta_{prop} = 0.7$, $\eta_{wrg} = 0.9$

With increased aspect ratio and reduced parasitic drag, as seen in Figure 18, the energy density relative to the aircraft's total mass tends to decrease. For year-round operation, an energy density of 150 Wh/kg is required. Assuming a usable battery energy density of 400 Wh/kg, about 40% of the aircraft's mass must be used for batteries. Based on the assumed wing loading of 5 kg/m², approximately 3 kg/m² remains for structural and system mass.

5. Summary and Outlook

This publication has addressed and discussed the fundamental design parameters of solar-electric stratospheric aircraft. It has been demonstrated that extreme lightweight construction is required for sustained flights in the stratosphere. However, the maximum permissible wing loadings vary depending on the aerodynamic efficiency of the design. Currently, two fundamentally different concepts are in development and flight testing: the Airbus Zephyr 8/S and the BAE PHASA-35. The Zephyr 8 is characterized by its extreme lightweight construction, while the PHASA-35 is noted for its high aerodynamic efficiency.

Evaluating these designs is beyond the scope of this publication. However, the choice of construction concept and the associated possibilities for achieving high aspect ratios and aerodynamic efficiency are such fundamental decisions at the beginning of a development project that they must be carefully weighed.

A critical factor for the economic viability and market success of solar-electric stratospheric aircraft is the cost of solar panels. For designs with lower aspect ratios, it has been shown that approximately 1.5 kg/m² of wing loading is available for structure and systems. Implementing such an aircraft with mass-market available monocrystalline silicon solar cells, even if their efficiency is further improved, will not be feasible. This is because such cells have surface weights of around 700 g/m², requiring significantly lighter, more expensive solar cells without significant economies of scale to provide sufficient mass budget for the remaining systems and structure. Even a substantial increase in battery energy density will not significantly change this.

For a design with a high aspect ratio, it is more realistic to use cost-effective mass-market solar cells through future increases in battery energy density. If the assumed battery energy density is raised from 400 Wh/kg to 550 Wh/kg, approximately 0.5 kg/m² of additional surface mass budget is gained at a constant energy density relative to the aircraft mass. This approximately corresponds to the mass difference between high-cost lightweight solar cells and mass-market solar cells.

6. Contact Author Email Address

Deutsches Zentrum für Luft- und Raumfahrt e.V.

Andreas Bierig Lilienthalplatz 7

D-38108 Braunschweig

mailto: Andreas.Bierig@dlr.de

7. Copyright Statement

The authors confirm that they, and/or their company or organization, hold copyright on all of the original material included in this paper. The authors also confirm that they have obtained permission, from the copyright holder of any third party material included in this paper, to publish it as part of their paper. The authors confirm that they give permission, or have obtained permission from the copyright holder of this paper, for the publication and distribution of this paper as part of the ICAS proceedings or as individual off-prints from the proceedings.

References

- [1] R. J. Boucher, "Sunrise, the world's first solar-powered airplane," *Journal of Aircraft*, vol. 22, no. 10, pp. 840–846, 1985, doi: 10.2514/3.45213.
- [2] NASA, "Pathfinder: Leading the way in solar flight," NASA, Edwards FS-2002-04-DFRC, 2002.
- [3] J. Levine, "A new record 96,863 feet," X-Press, 2002, 2002.
- [4] B. Tingley, So close! Zephyr drone lands just hours before setting flight-duration record. [Online]. Available: https://www.space.com/airbus-zephyr-drone-long-lands-before-record (accessed: Dec. 22 2023).
- [5] J. Brauchle, V. Gstaiger, S. Azimi, P. Dern, M. N. Mühlhaus, and F. Nikodem, "MACS-HAP: Design and Image Processing Features of the DLR HAP Camera System," in *International Geoscience and Remote Sensing Symposium*, Pasadena, CA, 2023.
- [6] M. Jirousek *et al.*, "Synthetic Aperture Radar Design for a High-Altitude Platform," in *14th European Conference on Synthetic Aperture Radar*, Leipzig, 2022.
- [7] C. Gueymard, "SMARTS2, A Simple Model of the Atmospheric Radiation Transfer of Sunshine: Algorithms and performance assessment," 1995. Accessed: Feb. 18 2024. [Online]. Available: https://www.fsec.ucf.edu/en/publications/pdf/fsec-pf-270-95.pdf
- [8] AIAA, Guide to Reference and Standard Atmosphere Models: G-003C-2010. Reston, 2010.
- [9] F. W. Leslie and C. G. Justus, "Earth Global Reference Atmospheric Model 2007 (Earth-GRAM07) Applications for the NASA Constellation Program," in *13th Conference on Aviation, Range and Aerospace Meteorology*, New Orleans, LA, 2008.
- [10] G. Arnason, *Airbus recognizes MicroLink as key supplier for Zephyr UAV platform*. [Online]. Available: https://financial-news.co.uk/airbus-recognizes-microlink-as-key-supplier-for-zephyr/ (accessed: May 17 2024).
- [11] NREL, Best Research-Cell Efficiency Chart. [Online]. Available: https://www.nrel.gov/pv/cell-efficiency.html (accessed: May 17 2024).
- [12] Y. Liang *et al.*, "A review of rechargeable batteries for portable electronic devices," *InfoMat*, vol. 1, no. 1, pp. 6–32, 2019, doi: 10.1002/inf2.12000.
- [13] P. Shepard, *Airbus Partners with Amprius for High Energy Density Battery Technology*. [Online]. Available: https://eepower.com/news/airbus-partners-with-amprius-for-high-energy-density-battery-technology/# (accessed: May 17 2024).
- [14] T. Robinson, *BAE Systems' Phasa-35 makes breakthrough stratospheric flight.* [Online]. Available: https://www.aerosociety.com/news/exclusive-bae-systems-phasa-35-makes-breakthrough-stratospheric-flight/